Microscopic calculations and energy expansions for neutron-rich matter

C Drischler, V. Soma, A Schwenk

Microscopic calculations and energy expansions for neutron-rich matter

C. Drischler,* V. Somà,† and A. Schwenk‡

Institut für Kernphysik, Technische Universität Darmstadt, 64289 Darmstadt, Germany

and ExtreMe Matter Institute EMMI, GSI Helmholtzzentrum für Schwerionenforschung GmbH, 64291 Darmstadt, Germany

(Received 21 October 2013; revised manuscript received 18 December 2013; published 21 February 2014)

We investigate asymmetric nuclear matter with two- and three-nucleon interactions based on chiral effective field theory, where three-body forces are fit only to light nuclei. Focusing on neutron-rich matter, we calculate the energy for different proton fractions and include estimates of the theoretical uncertainty. We use our *ab initio* results to test the quadratic expansion around symmetric matter with the symmetry energy term and confirm its validity for highly asymmetric systems. Our calculations are in remarkable agreement with an empirical parametrization for the energy density. These findings are very useful for astrophysical applications and for developing new equations of state.

DOI: 10.1103/PhysRevC.89.025806 PACS number(s): 21.65.Cd, 21.30.−x, 26.60.Kp

I. INTRODUCTION

Microscopic calculations of asymmetric nuclear matter are of great importance because of applications for nuclei and nuclear astrophysics, as well as from a general many-body theory perspective. Nuclei along isotopic chains span a considerable range of neutron-to-proton asymmetries, which influences many of their properties. In astrophysical environments, the equation of state of neutron-rich matter is key for core-collapse supernovae, neutron stars, and mergers of compact objects. Moreover, calculations of asymmetric matter can be used to guide nuclear energy-density functionals, in particular, for the evolution to neutron-rich systems.

While neutron matter and symmetric matter have been investigated extensively, there are few microscopic studies of asymmetric matter, because the phase space with different neutron and proton Fermi seas is more involved. The first microscopic calculation with simple interactions dates back to Brueckner, Coon, and Dabrowski [1]. This was followed by variational calculations with phenomenological two-nucleon (NN) and three-nucleon (3N) potentials [2], Brueckner-Hartree-Fock (BHF) calculations [3–6], auxiliary-field diffusion Monte Carlo with a simplified potential [7], and, at finite temperature, self-consistent Green's function methods [8]. Phenomenologically, one can also obtain information about the properties of asymmetric matter by using a quadratic expansion to interpolate between symmetric and neutron matter.

With the development of chiral effective field theory (EFT) to nuclear forces [9] and the renormalization group [10], which improves the many-body convergence, it is timely to revisit the study of asymmetric nuclear matter. Chiral EFT provides a systematic expansion for NN, 3N, and higher-body interactions with theoretical uncertainties. This is especially important for calculations of neutron-rich matter. Nuclear forces based on chiral EFT have been successfully used to study light to medium-mass nuclei, nuclear reactions, and nuclear matter [11]. In particular, neutron matter has been found to be perturbative for low-momentum interactions based on chiral EFT potentials [12] (see also Ref. [13] for symmetric matter), and the perturbative convergence was recently validated with first quantum Monte Carlo calculations for chiral EFT interactions [14]. For symmetric matter, the same low-momentum interactions predict realistic saturation properties within theoretical uncertainties using 3N forces fit only to light nuclei [15]. The properties of nucleonic matter were also studied using in-medium chiral perturbation theory approaches [16–19], lattice chiral EFT [20], and self-consistent Green's functions [21]. Finally, neutron matter was calculated completely to N^{3}LO including NN, 3N, and 4N interactions [22,23].

In this paper, we present the first calculations of asymmetric nuclear matter with NN and 3N interactions based on chiral EFT, which are fit only to few-body data. We focus on neutron-rich conditions and present results for the energy of asymmetric matter with proton fractions $x \leq 0.15$. In Sec. II, we discuss the NN and 3N interactions used, outline the calculational strategy, and give the different interaction contributions in asymmetric matter. Section III A presents our *ab initio* results for the energy of asymmetric matter, which we use to test the quadratic expansion and the symmetry energy in Sec. III B. In Sec. III C, we study an empirical parametrization of the energy, which was used in Ref. [24] to extend *ab initio* calculations of neutron matter to asymmetric matter for astrophysical applications. Finally, we conclude in Sec. IV.

II. FORMALISM

A. Nuclear Hamiltonian

We consider nuclear matter as an infinite, homogeneous system of neutrons and protons governed by a many-nucleon Hamiltonian,

$$H(\Lambda) = T + V_{\mathrm{NN}}(\Lambda) + V_{\mathrm{3N}}(\Lambda) + \ldots, \tag{1}$$

which depends on a resolution scale Λ. In this work, we include NN and 3N interactions based on chiral EFT [9,25]. To improve the many-body convergence [10], we evolve the

*cdrischler@theorie.ikp.physik.tu-darmstadt.de
†vittorio.soma@physik.tu-darmstadt.de
‡schwenk@physik.tu-darmstadt.de

TABLE I. Different sets of 3N couplings employed in the present calculations, taken from Ref. [15]. The values of the dimensionless c_D and c_E are fit to the ^{3}H binding energy, $E_{^3\mathrm{H}} = -8.482$ MeV, and the point charge radius of ^{4}He, $r_{^4\mathrm{He}} = 1.464$ fm for different NN/3N cutoffs and different c_i couplings. Λ and Λ_{3N} are in fm^{-1} and c_i values are in GeV^{-1}.

Set	Λ	Λ_{3N}	c_1	c_3	c_4	c_D	c_E
1	1.8	2.0	−0.8	−3.2	5.4	−1.621	−0.143
2	2.0	2.0	−0.8	−3.2	5.4	−1.705	−0.109
3	2.0	2.5	−0.8	−3.2	5.4	−0.230	−0.538
4	2.2	2.0	−0.8	−3.2	5.4	−1.575	−0.102
5	2.8	2.0	−0.8	−3.2	5.4	−1.463	−0.029
6	2.0	2.0	−0.8	−3.4	3.4	−4.381	−1.126
7	2.0	2.0	−0.8	−4.8	4.0	−2.632	−0.677

N^{3}LO 500 MeV NN potential of Ref. [26] to low-momentum interactions $V_{\mathrm{low}\,k}$ with a resolution scale $\Lambda = 1.8$–2.8 fm^{-1} and a smooth $n_{\mathrm{exp}} = 4$ regulator [27]. This follows the calculations of neutron and symmetric nuclear matter of Refs. [12,15].

At the 3N level, we include the leading N^{2}LO 3N forces [28,29], which consist of a long-range two-pion-exchange part V_c (with c_i couplings), an intermediate-range one-pion-exchange part V_D, and a short-range 3N contact interaction V_E:

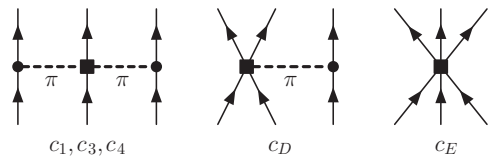

(2)

Their structures are given explicitly in Appendix B. As in Refs. [12,15], we use a smooth regulator, $f_R(p,q) = \exp[-((p^2 + 3q^2/4)/\Lambda_{3N}^2)^4]$, with Jacobi momenta p and q, which is symmetric under exchange of any particles. The c_D and c_E couplings were fit in Ref. [15] for given $V_{\mathrm{low}\,k}$, c_i couplings, and Λ/Λ_{3N} to the ^{3}H binding energy and the point charge radius of ^{4}He. This strategy has also been adopted to study exotic nuclei (see, e.g., Refs. [30,31]), with recent experimental highlights given in Refs. [32,33].

We consider the seven interaction sets listed in Table I, where the Λ/Λ_{3N} cutoffs and the c_i couplings are varied. This includes the consistent c_i values of the N^{3}LO 500 MeV NN potential of Ref. [26] (sets 1–5) and the c_i values from the N^{3}LO potentials of Ref. [34] (set 6) and from the NN partial-wave analysis (set 7) [35]. For the latter two c_i sets (6 and 7), the c_i couplings in the 3N force are not consistent with the NN interaction. For the purpose of this work, we consider the c_i variation as a probe of the uncertainty from higher-order long-range 3N forces (see Refs. [12,22,23]). For the results, we take the energy range given by these interaction sets as a measure of the theoretical uncertainty [12,15]. This probes the sensitivity to neglected higher-order short-range couplings (from cutoff variation) and the uncertainties in the long-range parts of 3N forces (from c_i variation). To improve upon this, future calculations will include the N^{3}LO 3N and 4N interactions following Refs. [22,23] and the consistent similarity renormalization-group evolution of 3N interactions in momentum space [36,37].

B. Calculational strategy

We focus on the calculation of asymmetric nuclear matter with a small proton fraction (for neutron-rich conditions). Our calculational scheme relies on the result that neutron matter is perturbative for low-momentum interactions [12], which was also shown recently for chiral EFT interactions with low cutoffs [22,23] and validated by quantum Monte Carlo [14]. Note that even the largest NN cutoff interaction (set 5) has been shown to be perturbative in symmetric nuclear matter [15]. We include NN and 3N interactions at the Hartree-Fock level and perturbative corrections to the energy density E/V from NN interactions at second order:

$$\frac{E_{\mathrm{NN}}}{V} \approx \frac{E^{(1)}_{\mathrm{NN}}}{V} + \frac{E^{(2)}_{\mathrm{NN}}}{V} \quad \text{and} \quad \frac{E_{\mathrm{3N}}}{V} \approx \frac{E^{(1)}_{\mathrm{3N}}}{V}. \tag{3}$$

This was found to be a reliable approximation for neutron matter [12]. In particular, note that second-order corrections involving 3N interactions have been shown to contribute only at the hundred keV level in neutron matter (see Table I in Ref. [12]).

Asymmetric nuclear matter is characterized by the neutron and proton densities, n_n and n_p, or, equivalently, by the proton fraction $x = n_p/n$ and the density $n = n_p + n_n$. In addition, we recall that for a given x, the proton and neutron Fermi momenta, k_F^p and k_F^n, and the density n are related by $k_F^p = k_F^n[x/(1-x)]^{1/3}$ and $n = (k_F^n)^3/[3\pi^2(1-x)]$.

We consider proton fractions $x \leq 0.15$. For such neutron-rich conditions, the contributions involving two and three protons are small, so that we approximate

$$\frac{E_{\mathrm{NN}}}{V} \approx \frac{E_{nn}}{V} + \frac{E_{np}}{V} \quad \text{and} \quad \frac{E_{\mathrm{3N}}}{V} \approx \frac{E_{nnn}}{V} + \frac{E_{nnp}}{V}. \tag{4}$$

As a check, we have evaluated the pp, ppn, and ppp contributions at the Hartree-Fock and second-order NN level. As discussed in the following, for the largest proton fraction considered ($x = 0.15$), these lead to energy contributions $[E_{pp} + E_{ppn} + E_{ppp}]/A = -0.2$ MeV at saturation density $n_0 = 0.16$ fm^{-3}, which are small compared to our uncertainty bands (see Fig. 1). We emphasize that closer to symmetric nuclear matter, the inclusion of higher-order many-body contributions will be important [15]. Work is under way to include these and to relax the approximation in the number of proton lines.

C. First-order NN contribution

The NN Hartree-Fock contribution to the energy density is given by

$$\frac{E^{(1)}_{\mathrm{NN}}}{V} = \frac{1}{2}\sum_{T,M_T}\int\frac{d\mathbf{k}}{(2\pi)^6}\left(\int d\mathbf{P}\, n^{\tau_1}_{\frac{\mathbf{P}}{2}+\mathbf{k}}\, n^{\tau_2}_{\frac{\mathbf{P}}{2}-\mathbf{k}}\right) \times \sum_{S,M_S}\langle \mathbf{k}SM_STM_T|\mathcal{A}_{12}V_{\mathrm{NN}}|\mathbf{k}SM_STM_T\rangle, \tag{5}$$

where $\mathbf{k} = (\mathbf{k}_1 - \mathbf{k}_2)/2$ and $\mathbf{P} = \mathbf{k}_1 + \mathbf{k}_2$ are the relative and center-of-mass momentum, $n^{\tau_i}_{\mathbf{k}_i}$ are the Fermi distribution

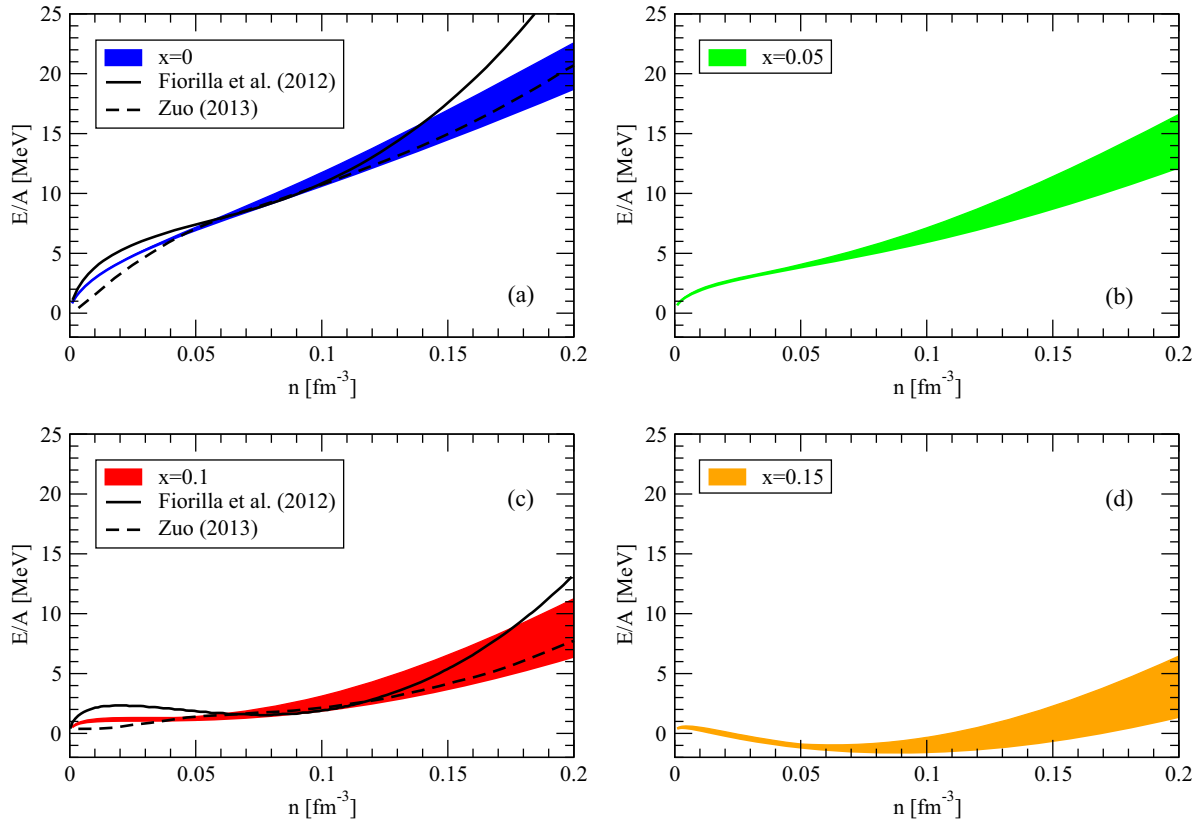

FIG. 1. (Color online) Energy per particle E/A of pure neutron matter ($x = 0$) and asymmetric nuclear matter for three proton fractions, $x = 0.05, 0.1$, and 0.15, as a function of density n. The bands estimate the uncertainty of our calculations (see text for details). Where available, we compare our results to the Brueckner-Hartree-Fock energies of Ref. [38] [Zuo (2013)] and to the energies obtained from in-medium chiral perturbation theory [Fiorilla *et al.* (2012)] [18].

functions of species $\tau_i = n, p$, and S and T denote the two-body spin and isospin, with projections M_S and M_T. For $M_T = 0$, Eq. (5) implies that $\tau_1 = n$ and $\tau_2 = p$. The energy involves a spin-summed antisymmetrized matrix element of the NN interaction with antisymmetrizer $\mathcal{A}_{12} = 1 - P_{12}$, where the particle-exchange operator $P_{12} = P_{12}^k P_{12}^\sigma P_{12}^\tau$ acts on momentum, spin, and isospin.

The integral over the center-of-mass momentum in Eq. (5) can be performed separately, as the NN interaction matrix element is independent of $\mathbf{P}$. The integration results in a function $f^{M_T}(k)$, which is given in Appendix A, Sec. 1. Expanding the NN matrix element in partial waves, the M_S sum can be performed explicitly. This gives, for the NN Hartree-Fock energy density,

$$\frac{E_{\rm NN}^{(1)}}{V} = \frac{1}{8\pi^4}\int_0^{\frac{k_F^n+k_F^p}{2}} dk\, k^2 \sum_{l,S,J}(2J+1) \times \Big[f^{nn}(k)\,\langle k|V_{l,l}^{J,S,M_T=-1}|k\rangle(1-(-1)^{l+S+1}) + f^{np}(k)\,\langle k|V_{l,l}^{J,S,M_T=0}|k\rangle(1-(-1)^{l+S}) + f^{np}(k)\,\langle k|V_{l,l}^{J,S,M_T=0}|k\rangle(1-(-1)^{l+S+1})\Big], \quad (6)$$

where we have neglected the pp contribution according to approximation (4) and $f^{M_T=0} \equiv f^{np}$. The orbital and total angular momentum are labeled l and J, respectively, and the factor $(1-(-1)^{l+S+T})$ takes into account the exchange term.

D. Second-order NN contribution

The second-order NN contribution to the energy density reads

$$\frac{E_{\rm NN}^{(2)}}{V} = \frac{1}{4}\sum_{S,M_S,M_{S'},T,M_T}\int \frac{d\mathbf{k}\,d\mathbf{k}'\,d\mathbf{P}}{(2\pi)^9} \times \frac{n_{\frac{\mathbf{P}}{2}+\mathbf{k}}^{\tau_1} n_{\frac{\mathbf{P}}{2}-\mathbf{k}}^{\tau_2}\left(1-n_{\frac{\mathbf{P}}{2}+\mathbf{k}'}^{\tau_3}\right)\left(1-n_{\frac{\mathbf{P}}{2}-\mathbf{k}'}^{\tau_4}\right)}{(k^2-k'^2)/m} \times |\langle \mathbf{k}SM_STM_T|\,\mathcal{A}_{12}V_{\rm NN}\,|\mathbf{k}'SM_S'TM_T\rangle|^2, \quad (7)$$

where $\mathbf{k}' = (\mathbf{k}_3 - \mathbf{k}_4)/2$ and we use an averaged nucleon mass $m = 938.92$ MeV. In addition, for $M_T = 0$ also $\tau_3 = n$ and $\tau_4 = p$. Expanding the NN matrix elements in partial waves and after spin sums, we have [12]

$$\sum_{S,M_S,M_S'}|\langle \mathbf{k}SM_STM_T|\,\mathcal{A}_{12}V_{\rm NN}\,|\mathbf{k}'SM_S'TM_T\rangle|^2 = \sum_{L,S}\sum_{J,l,l'}\sum_{\widetilde{J},\widetilde{l},\widetilde{l}'} P_L(\cos\theta_{\mathbf{k},\mathbf{k}'})(4\pi)^2\, i^{(l-l'+\widetilde{l}-\widetilde{l}')}\,(-1)^{\widetilde{l}+l'+L} \times \mathcal{C}_{l0\widetilde{l}'0}^{L0}\mathcal{C}_{l'0\widetilde{l}0}^{L0}\sqrt{(2l+1)(2l'+1)(2\widetilde{l}+1)(2\widetilde{l}'+1)}$$

$$\times (2J+1)(2\widetilde{J}+1)\begin{Bmatrix} l & S & J \\ \widetilde{J} & L & \widetilde{l}' \end{Bmatrix}\begin{Bmatrix} J & S & l' \\ \widetilde{l} & L & \widetilde{J} \end{Bmatrix}$$
$$\times \langle k|\, V_{l',l}^{J,S,M_T}\, |k'\rangle\, \langle k'|\, V_{\widetilde{l}',\widetilde{l}}^{\widetilde{J},S,M_T}\, |k\rangle$$
$$\times (1-(-1)^{l+S+T})(1-(-1)^{\widetilde{l}+S+T}), \quad (8)$$

with Legendre polynomial P_L, Clebsch-Gordan coefficients $\mathcal{C}$, and $6J$ symbols. We consider only the $L=0$ contribution in the partial-wave sum, (8), which is equivalent to angle averaging. The spin-summed NN matrix elements are then angle independent and the angular integrations over the Fermi distribution functions in Eq. (7) can be performed analytically, leading to the function

$$F^{M_T}(k,k',P) = \int d\Omega_{\mathbf{k}} \int d\Omega_{\mathbf{k}'} \int d\Omega_{\mathbf{P}} \times n^{\tau_1}_{\frac{\mathbf{P}}{2}+\mathbf{k}} n^{\tau_2}_{\frac{\mathbf{P}}{2}-\mathbf{k}} \left(1-n^{\tau_3}_{\frac{\mathbf{P}}{2}+\mathbf{k}'}\right)\left(1-n^{\tau_4}_{\frac{\mathbf{P}}{2}-\mathbf{k}'}\right), \quad (9)$$

which is derived in detail in Appendix A, Sec. 2. Combining this, we obtain for the second-order NN contribution to the energy density,

$$\frac{E^{(2)}_{\mathrm{NN}}}{V} = \frac{1}{4}\frac{1}{(2\pi)^9}\int_0^{k_F^n+k_F^p} dP\, P^2 \int_0^{\frac{k_F^n+k_F^p}{2}} dk\, k^2 \int_0^{\infty} dk'\, k'^2 \times \frac{m}{k^2-k'^2} \sum_{S,M_S,M_{S'},T,M_T} F^{M_T}(k,k',P) \times |\langle \mathbf{k} S M_S T M_T|\, \mathcal{A}_{12} V_{\mathrm{NN}}\, |\mathbf{k}' S M'_S T M_T\rangle|^2, \quad (10)$$

where the spin-isospin-summed matrix elements are given explicitly by Eq. (A4), which neglects the pp contributions, multiplied by the appropriate phase-space functions $F^{M_T}(k,k',P)$ in each channel.

E. First-order 3N contribution

The 3N Hartree-Fock contribution to the energy density is given by

$$\frac{E^{(1)}_{\mathrm{3N}}}{V} = \frac{1}{6}\mathrm{Tr}_{\sigma_1,\tau_1}\mathrm{Tr}_{\sigma_2,\tau_2}\mathrm{Tr}_{\sigma_3,\tau_3}\int \frac{d\mathbf{k}_1\, d\mathbf{k}_2\, d\mathbf{k}_3}{(2\pi)^9} \times n^{\tau_1}_{\mathbf{k}_1} n^{\tau_2}_{\mathbf{k}_2} n^{\tau_3}_{\mathbf{k}_3} f_{\mathrm{R}}^2\, \langle 123|\, \mathcal{A}_{123}\, V_{\mathrm{3N}}\, |123\rangle\,, \quad (11)$$

where $i \equiv \mathbf{k}_i, \sigma_i, \tau_i$ is a shorthand notation that includes all single-particle quantum numbers, f_R is the three-body regulator, and the three-body antisymmetrizer $\mathcal{A}_{123}$ is

$$\mathcal{A}_{123} = (1+P_{12}P_{23}+P_{13}P_{23})(1-P_{23}) = 1-P_{12}-P_{13}-P_{23}+P_{12}P_{23}+P_{13}P_{23}. \quad (12)$$

In the present work, we only include the contributions involving two or three neutrons owing to approximation (4). However, for isospin-symmetric interactions, the other contributions follow simply from exchanging neutrons with protons.

The contribution from three neutrons to the energy density, $E^{(1)}_{nnn}/V$ in Eq. (4), has been derived in the neutron matter calculation of Ref. [12]. In this case, the c_4 part of V_c and the V_D and V_E terms vanish (with the nonlocal regulator f_R) due to their isospin structure (c_4), the Pauli principle (V_E), and the coupling of pions to spin (V_D) [12]. For contributions involving two neutrons and a proton, $E^{(1)}_{nnp}/V$, all parts of the N^{2}LO 3N interactions enter. Their derivation is discussed in detail in Appendix B, where the final expressions for the V_c, V_D, and V_E parts are given by Eqs. (B17), (B21), and (B23). In summary, the 3N Hartree-Fock energy density neglecting the contributions from two and more proton lines is given by

$$\frac{E^{(1)}_{3N}}{V} = \frac{E^{(1)}_{V_c}}{V}\bigg|_{nnn} + 3\left(\frac{E^{(1)}_{V_c}}{V}+\frac{E^{(1)}_{V_D}}{V}+\frac{E^{(1)}_{V_E}}{V}\right)\bigg|_{nnp}. \quad (13)$$

III. RESULTS

A. Energy of asymmetric nuclear matter

We calculate the energy of asymmetric nuclear matter by evaluating Eqs. (6), (10), and (13) for densities $n \le 0.2$ fm^{-3} and proton fractions $x \le 0.15$. Our results for the energy per particle E/A are presented in Fig. 1 for pure neutron matter ($x=0$) and for three proton fractions ($x=0.05$, 0.1, and 0.15). As discussed in Sec. II A, we perform calculations for a range of cutoffs and c_i couplings, which gives an estimate of the theoretical uncertainty. This range is larger than the one from approximations in the many-body calculation [12,15]. In Fig. 1 and in the following, this uncertainty estimate is presented as energy bands. We emphasize that 3N forces are fit only to light nuclei and no parameters are adjusted to empirical nuclear matter properties.

The energy per particle in neutron matter has been benchmarked with the values reported in Ref. [12], with excellent agreement. For two proton fractions ($x=0$ and 0.1), we compare our energies to explicit calculations of asymmetric nuclear matter. The BHF results in Ref. [38] [Zuo (2013)] are based on the Argonne v_{18} supplemented by phenomenological 3N forces of Ref. [39]. While they exhibit an unusual behavior at low densities, they lie within our bands for densities $n \gtrsim 0.05$ fm^{-3}. In addition, we compare our energies with the results obtained from in-medium chiral perturbation theory [Fiorilla *et al.* (2012)] [18], which differ in their density dependence compared to our *ab initio* calculations. This could be caused by the approximation to the leading-order contact interactions in Ref. [18].

The interaction energies from NN and 3N contributions are shown separately in Fig. 2 for two proton fractions ($x=0$ and 0.1). We observe that the uncertainties from 3N forces dominate. This is consistent with the results for neutron matter [12] and can be improved by going to higher order in chiral EFT interactions and in the many-body calculation.

In order to assess an error estimate of our approximation, we have calculated the contributions involving two or more proton lines that are neglected in Eq. (4). For the different proton fractions at saturation density, we compare the central energy from the seven interaction sets in Table I evaluated at the same many-body level as Eq. (3). For $x=0.05$, 0.1, and 0.15, we obtain $E_{pp}/A = -0.2$ MeV (0.4%), -0.4 MeV (1.3%), and -0.9 MeV (2.4%), where the percentage number in parentheses is relative to the NN interaction energy. Similarly for the 3N contributions, $[E_{ppn}+E_{ppp}]/A = 0.1$ MeV (1.0%), 0.3 MeV (3.3%), and 0.6 MeV (7.2%), where the

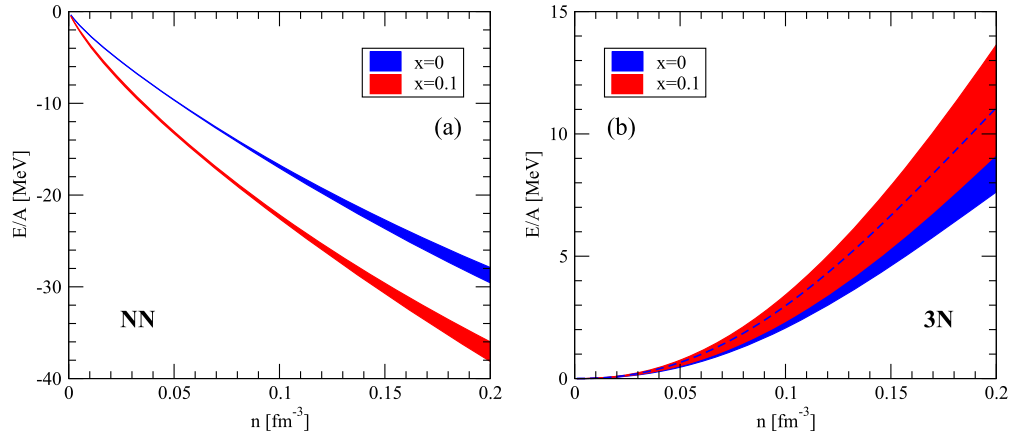

FIG. 2. (Color online) Interaction energy per particle from NN (a) and 3N (b) contributions for pure neutron matter (blue bands) and asymmetric nuclear matter with proton fraction $x = 0.1$ (red bands) as a function of density.

percentage number is relative to $[E_{nnn} + E_{nnp}]/A$. This shows that the neglected contributions from two or more proton lines are small. Furthermore, the NN and 3N contributions are opposite and, to a large extent, cancel in the total energy per particle. This confirms that approximation (4) works well for the neutron-rich conditions considered in this work. However, when we compare to constraints for the symmetry energy based on experiments around symmetric nuclei (see Fig. 4), we decided to include the small contributions from two or more proton lines. The corresponding changes in the symmetry energy are smaller than the theoretical uncertainties.

B. Quadratic expansion and symmetry energy

The technical difficulties of asymmetric matter calculations have triggered approximate or phenomenological expansions for the nuclear equation of state. Starting from the saturation point of symmetric matter, the quadratic expansion expresses the energy of asymmetric matter in terms of the asymmetry parameter $\beta = (n_n - n_p)/n = 1 - 2x$ as

$$\frac{E(n,\beta)}{A} = \frac{E(n,\beta=0)}{A} + S_v(n)\,\beta^2 + \mathcal{O}(\beta^4), \qquad (14)$$

where S_v is the symmetry energy. Provided that the equation of state of symmetric matter is known, S_v is the only input needed to extrapolate to asymmetric matter at order β^2. Originally designed for small values of β, the quadratic expansion has proven to be successful over a large range of asymmetries. Microscopic calculations have validated the β^2 truncation, with only small deviations away from symmetric matter [3,5].

We use our *ab initio* calculations to test the quadratic expansion for neutron-rich conditions. To this end, we define the energy difference from pure neutron matter ΔE:

$$\frac{\Delta E(n,x)}{A} = \frac{E(n,x)}{A} - \frac{E(n,x=0)}{A}. \qquad (15)$$

In terms of ΔE, the quadratic approximation (14) reads

$$-\frac{\Delta E(n,\beta)}{A} = \frac{E(n,\beta=1)}{A} - \frac{E(n,\beta)}{A} = E_{\rm sym}(n)\,(1-\beta^2), \qquad (16)$$

where $E_{\rm sym}$ coincides with the symmetry energy S_v, if $\mathcal{O}(\beta^4)$ terms vanish. Equation (16) allows us to extract $E_{\rm sym}$ for a given density and to verify the linearity in $(1-\beta^2)$. In Fig. 3, we show our results for $-\Delta E/A$ as a function of $(1-\beta^2)$ for three representative densities. For each value of β (or x), the vertical error bars reflect the energy range in Fig. 1. The colored bands in Fig. 3 are linear fits to the points with the corresponding errors. This demonstrates that the quadratic expansion is a very good approximation even for neutron-rich conditions.

From the slope of the linear fits in Fig. 3 one can extract $E_{\rm sym}$ for a given density. The resulting values for the three representative densities are listed in Table II. At saturation density, we find $E_{\rm sym} = 30.8 \pm 0.8$ MeV. Note that

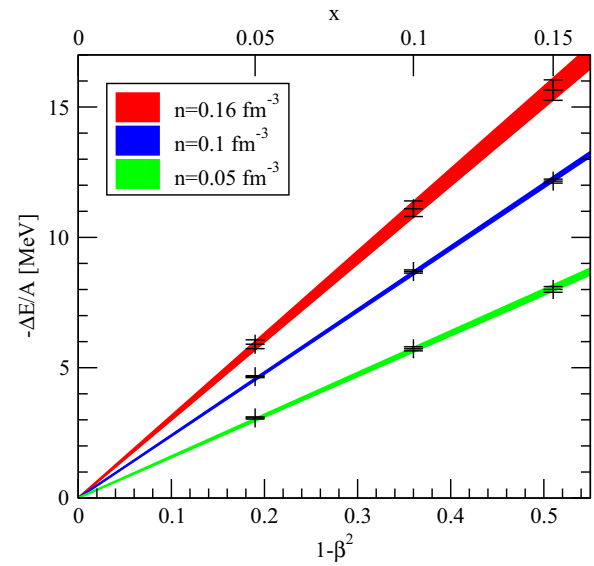

FIG. 3. (Color online) Energy per particle relative to pure neutron matter $-\Delta E/A$ as a function of $(1-\beta^2)$ for three densities; the upper axis gives the proton fraction x. The points correspond to our calculations, with error bars reflecting the uncertainty bands in Fig. 1. The colored bands are linear fits to the points with the corresponding errors.

TABLE II. $E_{\rm sym}$ and corresponding uncertainties extracted from the linear fits in Fig. 3 for the three densities.

n (fm^{-3})	$E_{\rm sym}$ (MeV)
0.05	15.8 ± 0.2
0.10	24.0 ± 0.2
0.16	30.8 ± 0.8

with the inclusion of the contributions from two or more proton lines, neglected in Eq. (4), $E_{\rm sym}$ slightly increases, to 31.2 ± 1.0 MeV. The uncertainty range is smaller than when extracting $E_{\rm sym}$ from neutron matter calculations and the empirical saturation point (see Refs. [12,24,43]). This is caused by the explicit information from asymmetric matter results.

Figure 4 shows $E_{\rm sym}$ as a function of density extracted from our asymmetric matter calculations as in Fig. 3. The $E_{\rm sym}$ band is caused by the theoretical uncertainty of our calculations for the energy. In this case, we have included the small contributions from two or more hole lines discussed above. Our results are compared in Fig. 4 with constraints from a recent analysis of isobaric analog states (IAS) and with inclusion of the constraints from neutron skins (IAS + skins) [42], showing a remarkable agreement over the entire density range. In addition, we show $E_{\rm sym}$ obtained from microscopic calculations performed with a variational approach [Akmal *et al.* (1998)] [40] and at the Brueckner-Hartree-Fock (BHF)

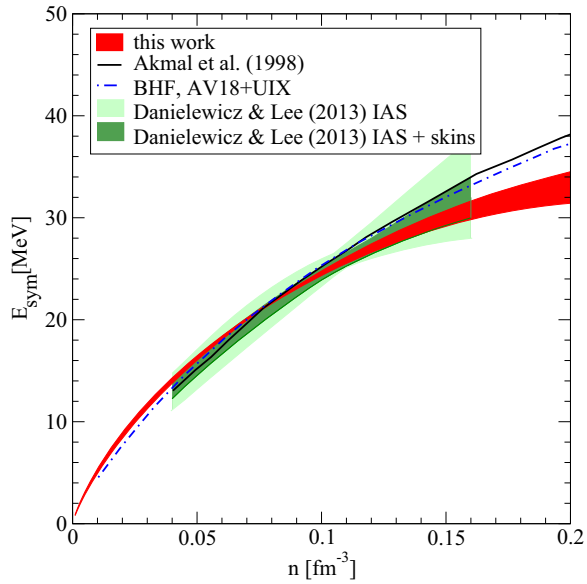

FIG. 4. (Color online) $E_{\rm sym}$ as a function of density obtained from our *ab initio* calculations as in Fig. 3, including the small contributions from two or more proton lines. In comparison, we give $E_{\rm sym}$ obtained from microscopic calculations performed with a variational approach [Akmal *et al.* (1998)] [40] and at the BHF level [41] based on the Argonne v_{18} NN and Urbana UIX 3N potentials (with parameters adjusted to the empirical saturation point). The band over the density range $n = 0.04$–0.16 fm^{-3} is based on a recent analysis of isobaric analog states (IAS) and with inclusion of the constraints from neutron skins (IAS + skins) [42].

level [41]. Both calculations are based on the Argonne v_{18} NN and Urbana UIX 3N potentials (with different parameters adjusted to the empirical saturation point), but derive $E_{\rm sym}$ from symmetric and pure neutron matter using the quadratic expansion (14). These results are compatible with our $E_{\rm sym}$ band at low and intermediate densities but predict a somewhat stiffer $E_{\rm sym}$ for $n \gtrsim n_0$. We attribute these differences to the phenomenological 3N forces used.

C. Empirical parametrization

In order to extend *ab initio* calculations of neutron matter to asymmetric matter for astrophysical applications, Ref. [24] used an empirical parametrization that represents an expansion in the Fermi momentum with kinetic energies plus interaction energies that follow the quadratic expansion with $x(1-x) = (1-\beta^2)/4$:

$$\frac{E(\overline{n},x)}{A} = T_0\Big[\frac{3}{5}(x^{5/3}+(1-x)^{5/3})(2\overline{n})^{2/3} - ((2\alpha-4\alpha_L)x(1-x)+\alpha_L)\,\overline{n} + ((2\eta-4\eta_L)x(1-x)+\eta_L)\,\overline{n}^{4/3}\Big], \quad (17)$$

where $\overline{n} = n/n_0$ denotes the density in units of saturation density and $T_0 = (3\pi^2 n_0/2)^{2/3}/(2m) = 36.84$ MeV is the Fermi energy at n_0. The parameters α, η, α_L, and η_L are determined from fits to neutron-matter calculations (α_L,η_L) and to the empirical saturation point of symmetric matter. The latter gives $\alpha = 5.87$, $\eta = 3.81$. The uncertainty range of α_L,η_L obtained from neutron-matter calculations is shown in Fig. 4 of Ref. [24].

We use our *ab initio* calculations to benchmark the empirical parametrization (17) for asymmetric matter. The comparison is shown in Fig. 5 for the energy difference from neutron matter $\Delta E/A$ as a function of density for three proton fractions. Remarkably, our results based on nuclear forces fit only to few-body data agree within uncertainties with the empirical parametrization (17) used in Ref. [24] to extrapolate from pure neutron matter to neutron-rich matter. We observe only a slight difference in the density dependence, with the empirical parametrization of Hebeler *et al.* [24] underestimating (overestimating) our band at lower (higher) densities.

We investigate whether the small discrepancy could be caused by the neutron effective mass m_n^* in the empirical expansion. To this end, we replace the kinetic part in Eq. (17) with

$$T_0\left[\frac{3}{5}\left(x^{5/3}+\frac{m}{m_n^*}(1-x)^{5/3}\right)(2\overline{n})^{2/3}\right], \quad (18)$$

while the terms proportional to $\overline{n}$ and $\overline{n}^{4/3}$ remain unchanged. For each proton fraction, we fit a density-dependent neutron effective mass m_n^*/m such that the difference between (the upper bands of) our microscopic calculation and the empirical parametrization with the modified kinetic term (18) is minimized. The values and ranges for α, η, α_L, and η_L are kept the same. In Fig. 6, we show the resulting m_n^*/m [Fig. 6(b)] and the improved empirical parametrization [Fig. 6(a)] for a

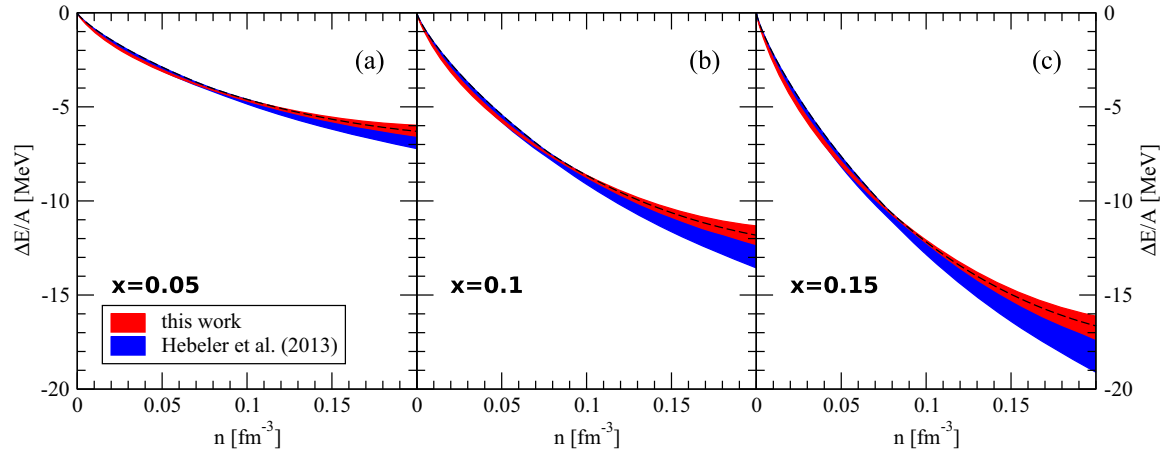

FIG. 5. (Color online) Energy per particle $\Delta E/A$ relative to pure neutron matter as a function of density for three proton fractions: $x = 0.05$, 0.1, and 0.15. The results of our calculations ("this work"; red bands) are compared with the empirical parametrization (17) used in Ref. [24] to extrapolate from pure neutron matter to neutron-rich matter [Hebeler *et al.* (2013), blue bands].

representative proton fraction $x = 0.1$. With the introduction of a weakly density-dependent neutron effective mass, the empirical parametrization agrees excellently with our *ab initio* results. Moreover, the behavior of m_n^*/m with a small increase at low densities and a decreasing effective mass with increasing density is in line with the expectations from microscopic calculations [44].

Finally, we discuss the possible factorization of the dependence on density and asymmetry in the energy of asymmetric nuclear matter. In the three panels in Fig. 5, one notes that increasing the proton fraction x approximately results in an overall rescaling of the density dependence of $\Delta E/A$.

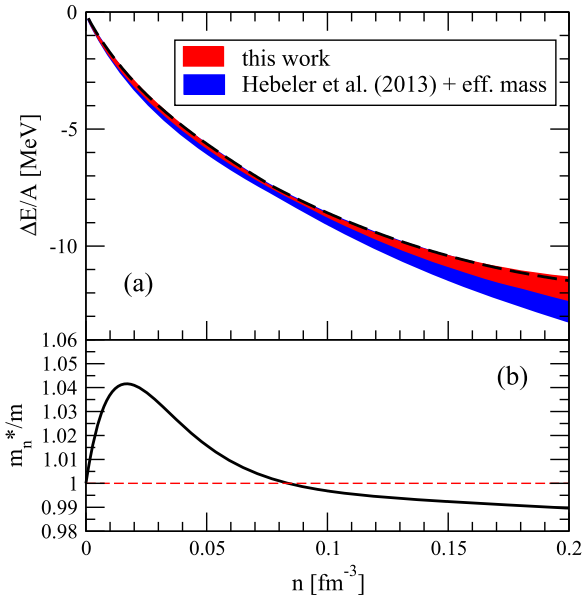

FIG. 6. (Color online) (a) Same as Fig. 5 for a proton fraction $x = 0.1$ but with the modified kinetic term (18) in the empirical parametrization (17). (b) Neutron effective mass m_n^*/m as a function of density obtained by fitting to $\Delta E/A$ in the upper panel (see text for details).

This rescaling suggests a factorization of the dependence on x and on the density: $\Delta E/A(n,x) = \Psi(x)\Phi(n)$. Such a factorization is explicit in the quadratic expansion, where $\Psi(x) = x(1-x) = (1-\beta^2)/4$ and $\Phi(n) = -4E_{\rm sym}(n)$; see Eq. (16). Assuming the same $\Psi(x) = x(1-x)$, we have checked whether a similar result holds for the empirical parametrization, (17). In this case, our *ab initio* results for $\Delta E/A$ are approximately reproduced for $x \leq 0.15$ by

$$\Phi(n) = T_0[-0.92\,(2\overline{n})^{2/3} - (2\alpha - 4\alpha_L)\,\overline{n} + (2\eta - 4\eta_L)\,\overline{n}^{4/3}]. \tag{19}$$

Using a central value of $\alpha_L = 1.33$ and $\eta_L = 0.88$ gives an $E_{\rm sym}(n) = -\Phi(n)/4$ that is very similar to our *ab initio* results in Fig. 4 and also lies within the experimental constraints from IAS and neutron skins [42].

IV. CONCLUSIONS

We have carried out the first calculations of asymmetric nuclear matter with NN and 3N interactions based on chiral EFT. The phase space owing to the different neutron and proton Fermi seas was handled without approximations. Focusing on neutron-rich conditions, we have presented results for the energy of asymmetric matter for different proton fractions (Fig. 1), including estimates of the theoretical uncertainty. As shown for neutron matter in Ref. [12], the energy range is dominated by the uncertainty in 3N forces (Fig. 2).

We have used our *ab initio* results to test the quadratic expansion around symmetric matter with the symmetry energy term. The comparison (Fig. 3) demonstrates that the quadratic approximation works very well even for neutron-rich conditions. In contrast to other calculations, our results are based on 3N forces fit only to light nuclei, without adjustments to empirical nuclear matter properties. Therefore, it is remarkable that the symmetry energy extracted from our *ab initio* calculations (Fig. 4) is in very good agreement with empirical constraints from IAS and neutron skins [42]. Moreover, compared to extracting the symmetry energy from neutron-matter calculations and the empirical saturation point,

the symmetry-energy uncertainty is reduced owing to the explicit information from asymmetric matter.

Finally, we have studied an empirical parametrization of the energy that represents an expansion in Fermi momentum with kinetic energies plus interaction energies that are quadratic in the asymmetry. This was used in Ref. [24] to extend *ab initio* calculations of neutron matter to asymmetric matter for astrophysical applications. Our asymmetric matter results are in remarkable agreement with this empirical parametrization (Fig. 5). This finding is very useful for describing neutron-rich conditions in astrophysics, for neutron star structure [24,43] and neutron star mergers [45], and for developing new equations of state for core-collapse supernovae.

The present calculations represent the first step in systematic predictions of asymmetric nuclear matter including theoretical uncertainties. This is very important in light of the many astrophysical applications. In the present work, we have limited our calculations to neutron-rich conditions with $x \leq 0.15$. Future work includes larger proton fractions, improvements in the many-body calculation, and the inclusion of higher-order interactions in chiral EFT. These are all possible owing to recent developments [14,22,23,36,37]. It is exciting that even at the current level, neutron-rich matter can be reliably calculated and the results provide important input for astrophysics. With the future improvements outlined above, we will then be able to narrow the energy bands further.

ACKNOWLEDGMENTS

We thank K. Hebeler and I. Tews for useful comments and discussions. This work was supported by the Helmholtz Alliance Program of the Helmholtz Association, contract HA216/EMMI "Extremes of Density and Temperature: Cosmic Matter in the Laboratory"; the DFG through Grant No. SFB 634; and ERC Grant No. 307986 STRONGINT.

APPENDIX A: ANGULAR INTEGRATIONS AND PARTIAL-WAVE DECOMPOSITION OF NN CONTRIBUTIONS

1. First-order NN contribution

We first consider the NN contribution to the Hartree-Fock energy, (5). The integral over the total momentum of the nucleon pair can be performed separately, as the interaction is independent of $\mathbf{P}$. Taking the direction of $\mathbf{k}$ along the z axis, the integration yields a function of k,

$$f^{np}(k) = \int d\mathbf{P}\, n^n_{\frac{\mathbf{P}}{2}+\mathbf{k}} n^p_{\frac{\mathbf{P}}{2}-\mathbf{k}}, \tag{A1}$$

where we consider the general case of different Fermi seas. The case of two neutrons/protons is then easily obtained.

The two Fermi distribution functions are equivalent to two spheres in momentum space, displaced by $\pm\mathbf{k}$ relative to the origin. Assuming $k_F^n \geq k_F^p$, there are three possible configurations depending on the value of k. The Fermi seas overlap partially, overlap totally, or do not overlap:

(1.1) $0 \leq k \leq \frac{k_F^n - k_F^p}{2}$;
(1.2) $\frac{k_F^n - k_F^p}{2} \leq k \leq \frac{k_F^n + k_F^p}{2}$; or

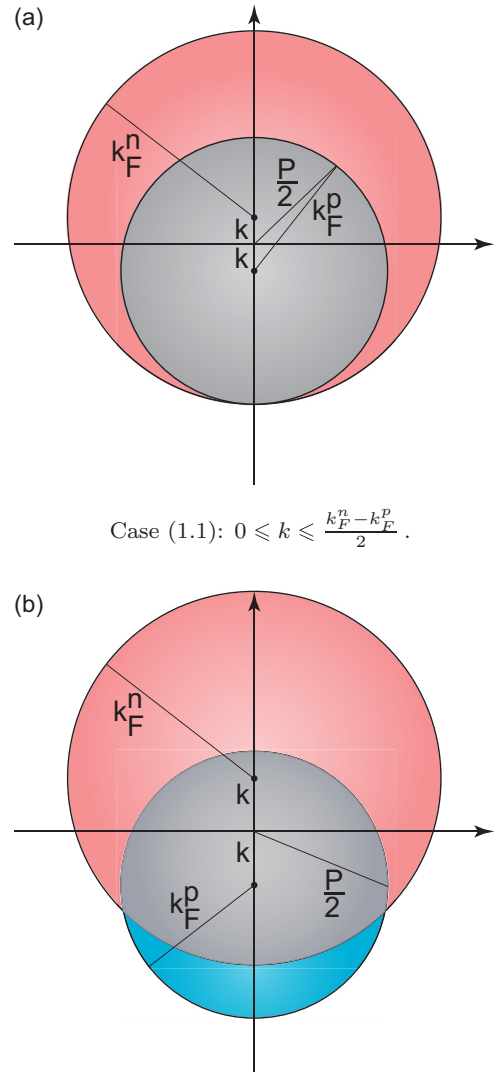

FIG. 7. (Color online) Different regions contributing to the integral (A1). As discussed in the text, there are three possible cases. The two nonvanishing cases are shown: the neutron (red) and proton (blue) Fermi seas overlap totally (a) or partially (b). Only the overlap (gray) contributes to the integral.

(1.3) $k \geq \frac{k_F^n + k_F^p}{2}$.

The first two cases are shown in Fig. 7. Case (1.3) is trivial because the integral vanishes. Here and in the following section, we give only the nonvanishing cases. The angular integration yields

$$f^{np}(k) = \begin{cases} \frac{32\pi}{3}\left(k_F^p\right)^3 & \text{for case (1.1),} \\ \frac{\pi}{3k}\left(-2k + k_F^n + k_F^p\right)^2 & \\ \quad \times\left[4k^2 + 4k\left(k_F^n + k_F^p\right)\right. & \\ \quad \left. - 3\left(k_F^n - k_F^p\right)^2\right] & \text{for case (1.2).} \end{cases} \tag{A2}$$

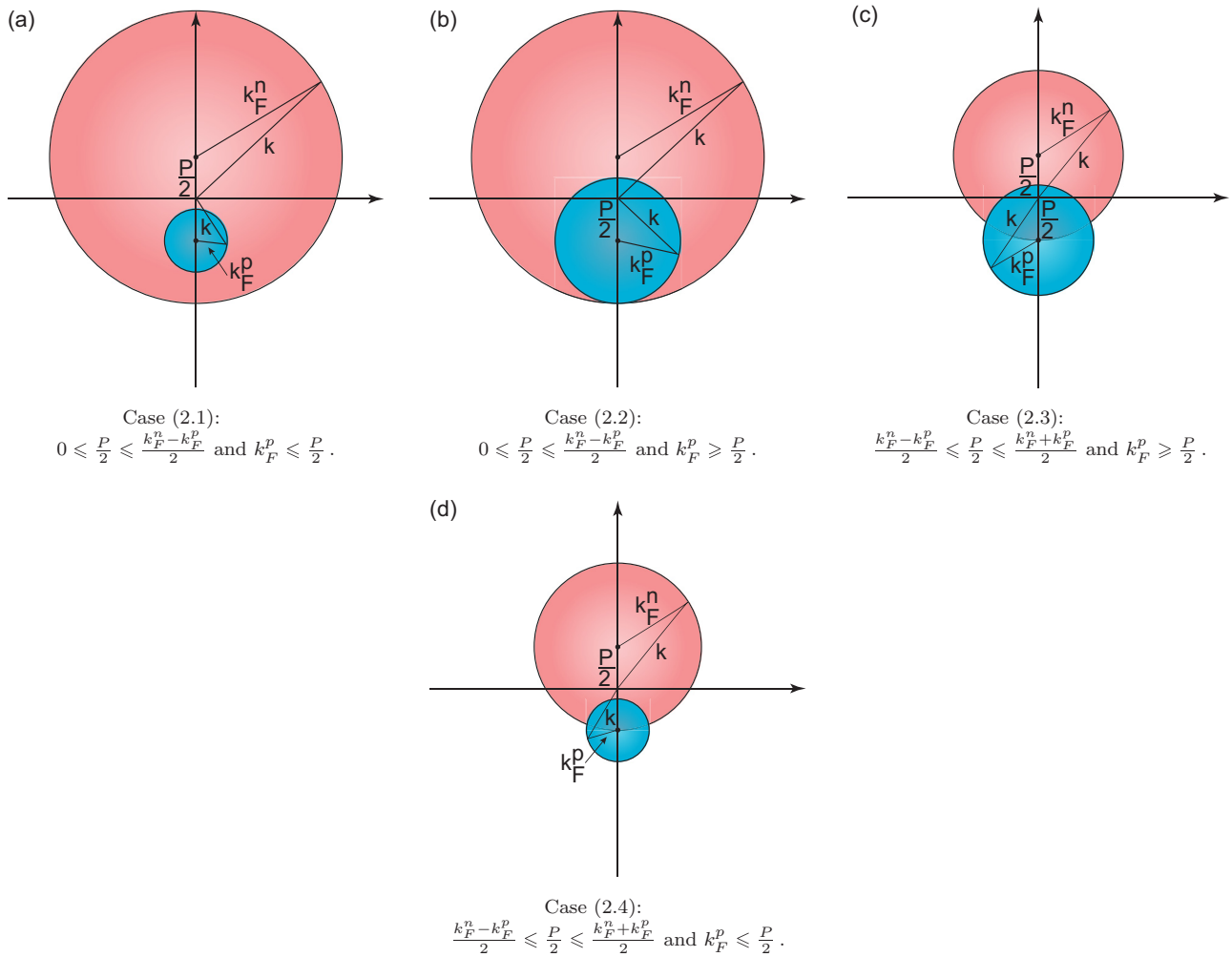

FIG. 8. (Color online) Different regions contributing to the integral (A8). Red (blue) spheres represent the neutron (proton) Fermi seas.

Case (1.1) is simply 8 (from $\mathbf{P}/2$) times the volume of the proton Fermi sea. Case (1.2) is identical to the hole-hole phase space at second order and can be obtained from cases (2.3) and (2.4) (upon exchanging $P/2$ and k and integrating over $\cos\theta_{\mathbf{k},\mathbf{P}}$ and P), which both give the result for case (1.2) above.

The NN interaction matrix element in Eq. (5) is expanded in partial waves, resulting in

$$\frac{E_{\rm NN}^{(1)}}{V} = \frac{1}{8\pi^4}\int_0^{\frac{k_F^n+k_F^p}{2}} dk\, k^2 \sum_{l,S,J,T,M_T} (2J+1) \times f^{M_T}(k)\,\langle k|V_{l,l}^{J,S,M_T}|k\rangle(1-(-1)^{l+S+T}), \quad \text{(A3)}$$

where $f^{M_T=0} \equiv f^{np}$. Writing out the sum over isospin states and neglecting the pp contribution [see Eq. (4)] leads to the NN Hartree-Fock energy (6).

2. Second-order NN contribution

We first expand the interaction matrix elements entering the second-order NN contribution (7) in partial waves. This generalizes Ref. [12] to arbitrary isospin asymmetries. After expanding the angular parts in spherical harmonics, taking $\mathbf{k}'$ along the z axis and $\mathbf{k}$ in the x-z plane, inserting $(-1)^{l+S+T}$ for each antisymmetrizer, and neglecting the pp contributions, we have

$$\begin{aligned}
&\sum_{S,M_S,M_S',T,M_T} |\langle \mathbf{k}SM_STM_T|\,\mathcal{A}_{12}V_{\rm NN}\,|\mathbf{k}'SM_S'TM_T\rangle|^2 \\
&= \sum_{L,S}\sum_{J,l,l'}\sum_{\widetilde{J},\widetilde{l},\widetilde{l}'} P_L(\cos\theta_{\mathbf{k},\mathbf{k}'})(4\pi)^2\, i^{(l-l'+\widetilde{l}-\widetilde{l}')}\,(-1)^{\widetilde{l}+l'+L} \\
&\times \mathcal{C}^{L0}_{l0\widetilde{l}'0}\mathcal{C}^{L0}_{l'0\widetilde{l}0}\sqrt{(2l+1)(2l'+1)(2\widetilde{l}+1)(2\widetilde{l}'+1)} \\
&\times (2J+1)(2\widetilde{J}+1)\begin{Bmatrix} l & S & J \\ \widetilde{J} & L & \widetilde{l}' \end{Bmatrix}\begin{Bmatrix} J & S & l' \\ \widetilde{l} & L & \widetilde{J} \end{Bmatrix} \\
&\times \Big[\langle k|\, V_{l',l}^{J,S,M_T=-1}\,|k'\rangle\,\langle k'|\, V_{\widetilde{l}',\widetilde{l}}^{\widetilde{J},S,M_T=-1}\,|k\rangle \\
&\times(1-(-1)^{l+S+1})(1-(-1)^{\widetilde{l}+S+1}) \\
&+ \langle k|\, V_{l',l}^{J,S,M_T=0}\,|k'\rangle\,\langle k'|\, V_{\widetilde{l}',\widetilde{l}}^{\widetilde{J},S,M_T=0}\,|k\rangle \\
&\times(1-(-1)^{l+S})(1-(-1)^{\widetilde{l}+S}) \\
&+ \langle k|\, V_{l',l}^{J,S,M_T=0}\,|k'\rangle\,\langle k'|\, V_{\widetilde{l}',\widetilde{l}}^{\widetilde{J},S,M_T=0}\,|k\rangle \\
&\times(1-(-1)^{l+S+1})(1-(-1)^{\widetilde{l}+S+1})\Big]. \qquad \text{(A4)}
\end{aligned}$$

Some of the integrals in Eq. (7) can be performed analytically. The angular integrations over the Fermi distribution functions give rise to a function of the magnitude of the momenta,

$$F^{np}(k,k',P) = \int d\Omega_{\mathbf{k}} \int d\Omega_{\mathbf{k}'} \int d\Omega_{\mathbf{P}} \times n^n_{\frac{\mathbf{P}}{2}+\mathbf{k}}\, n^p_{\frac{\mathbf{P}}{2}-\mathbf{k}} \left(1-n^n_{\frac{\mathbf{P}}{2}+\mathbf{k}'}\right)\left(1-n^p_{\frac{\mathbf{P}}{2}-\mathbf{k}'}\right), \tag{A5}$$

which is then used in Eq. (10). Again, we focus on the np case. To derive $F^{np}(k,k',P)$, let us take $\mathbf{P}$ along the z axis and $\mathbf{k}$ in the x-z plane. We consider only the $L=0$ contribution in the partial-wave expression (A4) which is equivalent to angle averaging. In this approximation, the $\varphi_{\mathbf{k}'}$ integration yields 2π and we are left with

$$F^{np}(k,k',P) = 16\pi^3 \int_{-1}^{1} d\cos\theta_{\mathbf{k},\mathbf{P}} \int_{-1}^{1} d\cos\theta_{\mathbf{k}',\mathbf{P}} \times n^n_{\frac{\mathbf{P}}{2}+\mathbf{k}}\, n^p_{\frac{\mathbf{P}}{2}-\mathbf{k}} \left(1-n^n_{\frac{\mathbf{P}}{2}+\mathbf{k}'}\right)\left(1-n^p_{\frac{\mathbf{P}}{2}-\mathbf{k}'}\right). \tag{A6}$$

The two integrals can be worked out separately, giving rise to two functions that account for the hole-hole (hh) and particle-particle (pp) phase space

$$F^{np}(k,k',P) = 16\pi^3 F^{np}_{\rm hh}(k,P)\, F^{np}_{\rm pp}(k',P). \tag{A7}$$

Let us start with the hole-hole part. This is given by the volume of the intersection of two Fermi spheres with radii k^n_F and k^p_F whose centers are displaced by $\mathbf{P}$. Depending on the value of P, one has to distinguish four cases, which are shown in Fig. 8:

(2.1) $0 \le \frac{P}{2} \le \frac{k^n_F - k^p_F}{2}$ and $k^p_F \le \frac{P}{2}$;
(2.2) $0 \le \frac{P}{2} \le \frac{k^n_F - k^p_F}{2}$ and $k^p_F \ge \frac{P}{2}$;
(2.3) $\frac{k^n_F - k^p_F}{2} \le \frac{P}{2} \le \frac{k^n_F + k^p_F}{2}$ and $k^p_F \ge \frac{P}{2}$; and
(2.4) $\frac{k^n_F - k^p_F}{2} \le \frac{P}{2} \le \frac{k^n_F + k^p_F}{2}$ and $k^p_F \le \frac{P}{2}$.

It is useful to express the function $F^{np}_{\rm hh}(k,P)$ as

$$F^{np}_{\rm hh}(k,P) = \int_{f_1(k,P)}^{f_2(k,P)} d\cos\theta_{\mathbf{k},\mathbf{P}}\, n^n_{\frac{\mathbf{P}}{2}+\mathbf{k}}\, n^p_{\frac{\mathbf{P}}{2}-\mathbf{k}}, \tag{A8}$$

where the lower and upper limits of the integration will be different in each case. In the first two total-overlap cases, one has $f_1(k,P) = -1$, and for case (2.1)

$$f_2(k,P) = \begin{cases} -1, & k \le \frac{P}{2} - k^p_F, \\ \frac{(k^p_F)^2 - (\frac{P}{2})^2 - k^2}{2k\frac{P}{2}}, & \frac{P}{2} - k^p_F \le k \le k^p_F + \frac{P}{2}, \\ -1, & k \ge k^p_F + \frac{P}{2}, \end{cases} \tag{A9}$$

while for case (2.2)

$$f_2(k,P) = \begin{cases} 1, & k \le k^p_F - \frac{P}{2}, \\ \frac{(k^p_F)^2 - (\frac{P}{2})^2 - k^2}{2k\frac{P}{2}}, & k^p_F - \frac{P}{2} \le k \le k^p_F + \frac{P}{2}, \\ -1, & k \ge k^p_F + \frac{P}{2}. \end{cases} \tag{A10}$$

The partial overlap cases yield more involved integration limits. We find, for case (2.3),

$$f_1(k,P) = \begin{cases} -1, & k \le k^n_F - \frac{P}{2}, \\ \frac{(k^n_F)^2 - (\frac{P}{2})^2 - k^2}{-2k\frac{P}{2}}, & k^n_F - \frac{P}{2} \le k \le k_0, \\ -1, & k \ge k_0 \end{cases} \tag{A11}$$

and

$$f_2(k,P) = \begin{cases} 1, & k \le k^p_F - \frac{P}{2}, \\ \frac{(k^p_F)^2 - (\frac{P}{2})^2 - k^2}{2k\frac{P}{2}}, & k^p_F - \frac{P}{2} \le k \le k_0, \\ -1, & k \ge k_0, \end{cases} \tag{A12}$$

where $k_0 = \sqrt{\frac{(k^n_F)^2 + (k^p_F)^2}{2} - \left(\frac{P}{2}\right)^2}$. Case (2.4) gives

$$f_1(k,P) = \begin{cases} -1, & k \le k^n_F - \frac{P}{2}, \\ \frac{(k^n_F)^2 - (\frac{P}{2})^2 - k^2}{-2k\frac{P}{2}}, & k^n_F - \frac{P}{2} \le k \le k_0, \\ -1, & k \ge k_0 \end{cases} \tag{A13}$$

and

$$f_2(k,P) = \begin{cases} -1, & k \le \frac{P}{2} - k^p_F, \\ \frac{(k^p_F)^2 - (\frac{P}{2})^2 - k^2}{2k\frac{P}{2}}, & \frac{P}{2} - k^p_F \le k \le k_0, \\ -1, & k \ge k_0. \end{cases} \tag{A14}$$

The second integral in Eq. (A6) is performed similarly, with the difference that now the volume excluded by the union of the two Fermi spheres contributes. One can distinguish two cases,

(3.1) $0 \le \frac{P}{2} \le \frac{k^n_F - k^p_F}{2}$ and
(3.2) $\frac{k^n_F - k^p_F}{2} \le \frac{P}{2} \le \frac{k^n_F + k^p_F}{2}$,

which are shown in Fig. 9. As for the hole-hole cases, we express the function $F^{np}_{\rm pp}(k',P)$ as

$$F^{np}_{\rm pp}(k',P) = \int_{f_1(k',P)}^{f_2(k',P)} d\cos\theta_{\mathbf{k}',\mathbf{P}} \left(1-n^n_{\frac{\mathbf{P}}{2}+\mathbf{k}'}\right)\left(1-n^p_{\frac{\mathbf{P}}{2}-\mathbf{k}'}\right). \tag{A15}$$

In the total overlap case (3.1), we have $f_1(k',P) = -1$ and

$$f_2(k',P) = \begin{cases} -1, & k' \le k^n_F - \frac{P}{2}, \\ \frac{(k^n_F)^2 - (\frac{P}{2})^2 - k'^2}{-2k'\frac{P}{2}}, & k^n_F - \frac{P}{2} \le k' \le k^n_F + \frac{P}{2}, \\ 1, & k' \ge k^n_F + \frac{P}{2}. \end{cases} \tag{A16}$$

The partial overlap case (3.2) yields

$$f_1(k',P) = \begin{cases} -1, & k' \le k_0, \\ \frac{(k^p_F)^2 - (\frac{P}{2})^2 - k'^2}{2k'\frac{P}{2}}, & k_0 \le k' \le k^p_F + \frac{P}{2}, \\ -1, & k' \ge k^p_F + \frac{P}{2} \end{cases} \tag{A17}$$

and

$$f_2(k',P) = \begin{cases} -1, & k' \le k_0, \\ \frac{(k^n_F)^2 - (\frac{P}{2})^2 - k'^2}{-2k'\frac{P}{2}}, & k_0 \le k' \le \frac{P}{2} + k^n_F, \\ 1, & k' \ge k^n_F + \frac{P}{2}. \end{cases} \tag{A18}$$

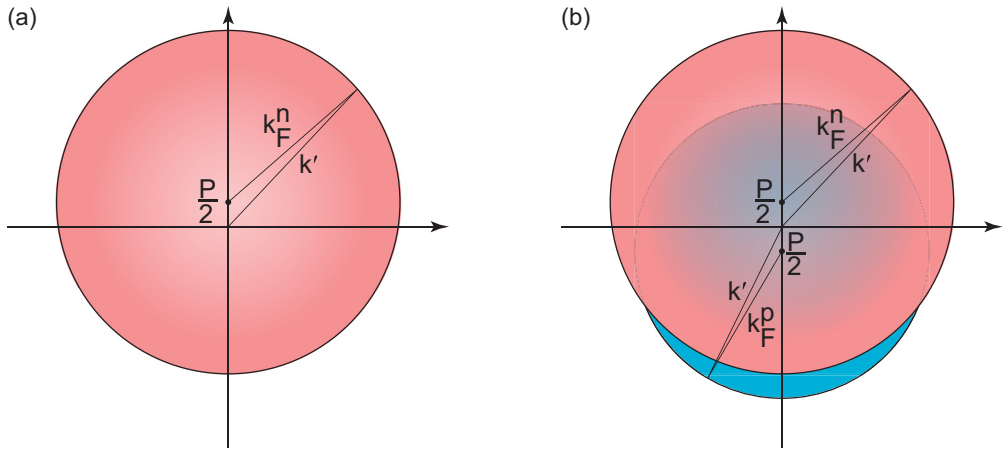

FIG. 9. (Color online) Different regions contributing to the integral (A15). Red (blue) spheres represent the neutron (proton) Fermi seas.

APPENDIX B: FIRST-ORDER 3N CONTRIBUTION

Next, we discuss the contributions from N^{2}LO 3N forces $V_{3N} = V_c + V_D + V_E$ and calculate the Hartree-Fock energy density (11). The different 3N interaction parts read [28,29]

$$V_c = \frac{1}{2}\left(\frac{g_A}{2F_\pi}\right)^2 \sum_{i\neq j\neq k} \frac{(\boldsymbol{\sigma}_i\cdot\mathbf{q}_i)(\boldsymbol{\sigma}_j\cdot\mathbf{q}_j)}{(q_i^2+m_\pi^2)(q_j^2+m_\pi^2)} F_{ijk}^{\alpha\beta}\,\tau_i^\alpha\,\tau_j^\beta, \tag{B1}$$

$$V_D = -\frac{g_A}{8F_\pi^2}\frac{c_D}{F_\pi^2\Lambda_\chi}\sum_{i\neq j\neq k}\frac{\boldsymbol{\sigma}_j\cdot\mathbf{q}_j}{q_j^2+m_\pi^2}(\boldsymbol{\sigma}_i\cdot\mathbf{q}_j)(\boldsymbol{\tau}_i\cdot\boldsymbol{\tau}_j), \tag{B2}$$

$$V_E = \frac{c_E}{2F_\pi^4\Lambda_\chi}\sum_{j\neq k}(\boldsymbol{\tau}_j\cdot\boldsymbol{\tau}_k), \tag{B3}$$

with $g_A = 1.29$, $F_\pi = 92.4$ MeV, $m_\pi = 138.04$ MeV, and $\Lambda_\chi = 700$ MeV. $\mathbf{q}_i = \mathbf{k}_i' - \mathbf{k}_i$ is the difference between initial and final nucleon momenta and

$$F_{ijk}^{\alpha\beta} = \delta^{\alpha\beta}\left[-\frac{4c_1m_\pi^2}{F_\pi^2} + \frac{2c_3}{F_\pi^2}\,\mathbf{q}_i\cdot\mathbf{q}_j\right] + \sum_\gamma \frac{c_4}{F_\pi^2}\,\epsilon^{\alpha\beta\gamma}\,\tau_k^\gamma\,\boldsymbol{\sigma}_k\cdot(\mathbf{q}_i\times\mathbf{q}_j). \tag{B4}$$

We consider the different 3N contributions for the *nnp* case according to approximation (4). The *nnn* expressions are given in Ref. [12].

1. V_c contribution

Let us write Eq. (B1) as

$$V_c = \frac{1}{2}\left(\frac{g_A}{2F_\pi}\right)^2\left(G^{(1)} + \frac{c_4}{F_\pi^2}\,G^{(2)}\right), \tag{B5}$$

with

$$G^{(1)} = \sum_{i\neq j\neq k} f_{ij}\,(\boldsymbol{\tau}_i\cdot\boldsymbol{\tau}_j), \tag{B6}$$

$$G^{(2)} = \sum_{i\neq j\neq k} g_{ij}\,\boldsymbol{\tau}_k\cdot(\boldsymbol{\tau}_i\times\boldsymbol{\tau}_j)\,\boldsymbol{\sigma}_k\cdot(\mathbf{q}_i\times\mathbf{q}_j), \tag{B7}$$

and

$$f_{ij} = \frac{(\boldsymbol{\sigma}_i\cdot\mathbf{q}_i)(\boldsymbol{\sigma}_j\cdot\mathbf{q}_j)}{(q_i^2+m_\pi^2)(q_j^2+m_\pi^2)}\left[-\frac{4c_1m_\pi^2}{F_\pi^2} + \frac{2c_3}{F_\pi^2}\,\mathbf{q}_i\cdot\mathbf{q}_j\right], \tag{B8}$$

$$g_{ij} = \frac{(\boldsymbol{\sigma}_i\cdot\mathbf{q}_i)(\boldsymbol{\sigma}_j\cdot\mathbf{q}_j)}{(q_i^2+m_\pi^2)(q_j^2+m_\pi^2)}. \tag{B9}$$

We need to calculate the matrix element $\langle 123|\mathcal{A}_{123}V_c|123\rangle$, with three-body antisymmetrizer

$$\mathcal{A}_{123} = 1 - P_{12} - P_{13} - P_{23} + P_{12}P_{23} + P_{13}P_{23}, \tag{B10}$$

where the particle-exchange operator acts on momentum, spin, and isospin $P_{ij} = P_{ij}^k\,P_{ij}^\sigma\,P_{ij}^\tau$. We first consider the isospin-exchange operators P_{ij}^τ for the $G^{(1)}$ part:

$$\begin{aligned}
&\langle nnp|\mathcal{A}_{123}G^{(1)}|nnp\rangle \\
&= \langle nnp|\sum_{i\neq j\neq k} f_{ij}(\boldsymbol{\tau}_i\cdot\boldsymbol{\tau}_j)|nnp\rangle \\
&-\langle nnp|P_{12}^{\sigma k}\sum_{i\neq j\neq k} f_{ij}(\boldsymbol{\tau}_i\cdot\boldsymbol{\tau}_j)|nnp\rangle \\
&-\langle pnn|P_{13}^{\sigma k}\sum_{i\neq j\neq k} f_{ij}(\boldsymbol{\tau}_i\cdot\boldsymbol{\tau}_j)|nnp\rangle \\
&-\langle npn|P_{23}^{\sigma k}\sum_{i\neq j\neq k} f_{ij}(\boldsymbol{\tau}_i\cdot\boldsymbol{\tau}_j)|nnp\rangle \\
&+\langle npn|P_{12}^{\sigma k}P_{23}^{\sigma k}\sum_{i\neq j\neq k} f_{ij}(\boldsymbol{\tau}_i\cdot\boldsymbol{\tau}_j)|nnp\rangle \\
&+\langle pnn|P_{13}^{\sigma k}P_{23}^{\sigma k}\sum_{i\neq j\neq k} f_{ij}(\boldsymbol{\tau}_i\cdot\boldsymbol{\tau}_j)|nnp\rangle.
\end{aligned} \tag{B11}$$

Evaluating the matrix elements for the different $\boldsymbol{\tau}_i \cdot \boldsymbol{\tau}_j$, we find

$$\begin{aligned}&\langle nnp|\mathcal{A}_{123}G^{(1)}|nnp\rangle\\&= 2\big[(f_{12}-f_{13}-f_{23}) - P_{12}^{\sigma k}(f_{12}-f_{13}-f_{23})\\&- 2P_{13}^{\sigma k}f_{13} - 2P_{23}^{\sigma k}f_{23} + 2P_{12}^{\sigma k}P_{23}^{\sigma k}f_{23} + 2P_{13}^{\sigma k}P_{23}^{\sigma k}f_{13}\big].\end{aligned} \tag{B12}$$

In the same way the $G^{(2)}$ part yields matrix elements of triple products, $\langle nnp|\boldsymbol{\tau}_1\cdot(\boldsymbol{\tau}_2\times\boldsymbol{\tau}_3)|nnp\rangle$, and permutations thereof. These can be evaluated using, for example,

$$\langle nnp|\epsilon^{\alpha\beta\gamma}\tau_1^\alpha\tau_2^\beta\tau_3^\gamma|nnp\rangle = \langle nnp|\epsilon^{zz\gamma}\tau_1^z\tau_2^z\tau_3^\gamma|nnp\rangle = 0, \tag{B13}$$

$$\langle npn|\epsilon^{\alpha\beta\gamma}\tau_1^\alpha\tau_2^\beta\tau_3^\gamma|nnp\rangle = \langle npn|\epsilon^{z\beta\gamma}\tau_1^z\tau_2^\beta\tau_3^\gamma|nnp\rangle = -2i. \tag{B14}$$

We then consider the spin-exchange part. The spin-exchange operator is given by $P_{ij}^\sigma = (1+\boldsymbol{\sigma}_i\cdot\boldsymbol{\sigma}_j)/2$. When summing over spins, only terms without Pauli matrices give nonvanishing contributions. For example, for the f_{ij} part, this leaves terms like

$$\begin{aligned}\big(\sigma_1^a\sigma_2^a\big)\big(\sigma_1^b q_1^b\big)\big(\sigma_2^c q_2^c\big) &= \big(\delta^{ab}+i\epsilon^{abd}\sigma_1^d\big)\big(\delta^{ac}+i\epsilon^{ace}\sigma_2^e\big)q_1^b q_2^c\\&\xrightarrow{\text{Tr}} 8\,\delta^{bc}q_1^b q_2^c = 8\,\mathbf{q}_1\cdot\mathbf{q}_2,\end{aligned} \tag{B15}$$

where the second line is given after tracing over the three spins in Eq. (11). For the same reason, this leaves for the g_{ij} part terms like

$$\begin{aligned}&\big(\sigma_1^a\sigma_2^a\big)\big(\sigma_2^b\sigma_3^b\big)\big(\sigma_1^c q_1^c\big)\big(\sigma_2^d q_2^d\big)\,\sigma_3^e(\mathbf{q}_1\times\mathbf{q}_2)^e\\&\xrightarrow{\text{Tr}} -8\,i\epsilon^{cdb}\,q_1^c\,q_2^d\,(\mathbf{q}_1\times\mathbf{q}_2)^b = -8\,i(\mathbf{q}_1\times\mathbf{q}_2)^2.\end{aligned} \tag{B16}$$

We then apply the momentum-exchange operator and evaluate $\mathbf{q}_i = \mathbf{k}_i' - \mathbf{k}_i$, where $\mathbf{k}_i'$ corresponds to the bra and $\mathbf{k}_i$ to the ket state. As a result, the V_c contribution to the Hartree-Fock energy density (11) is given by

$$\begin{aligned}\left.\frac{E_{V_c}^{(1)}}{V}\right|_{nnp} &= \frac{4}{3}\left(\frac{g_A}{2F_\pi}\right)^2\int\frac{d\mathbf{k}_1 d\mathbf{k}_2 d\mathbf{k}_3}{(2\pi)^9}\,n_{\mathbf{k}_1}^n n_{\mathbf{k}_2}^n n_{\mathbf{k}_3}^p\,f_{\mathrm{R}}^2\\&\times\Bigg(-\frac{4c_1m_\pi^2}{F_\pi^2}\left[\frac{k_{12}^2}{\big(k_{12}^2+m_\pi^2\big)^2}+\frac{k_{23}^2}{\big(k_{23}^2+m_\pi^2\big)^2}+\frac{k_{13}^2}{\big(k_{13}^2+m_\pi^2\big)^2}-\frac{\mathbf{k}_{23}\cdot\mathbf{k}_{31}}{\big(k_{23}^2+m_\pi^2\big)\big(k_{13}^2+m_\pi^2\big)}\right]\\&-\frac{2c_3}{F_\pi^2}\left[\frac{k_{12}^4}{\big(k_{12}^2+m_\pi^2\big)^2}+\frac{k_{23}^4}{\big(k_{23}^2+m_\pi^2\big)^2}+\frac{k_{13}^4}{\big(k_{13}^2+m_\pi^2\big)^2}-\frac{(\mathbf{k}_{23}\cdot\mathbf{k}_{31})^2}{\big(k_{23}^2+m_\pi^2\big)\big(k_{13}^2+m_\pi^2\big)}\right]\\&-\frac{c_4}{F_\pi^2}\left[\frac{(\mathbf{k}_{12}\times\mathbf{k}_{23})^2}{\big(k_{12}^2+m_\pi^2\big)\big(k_{23}^2+m_\pi^2\big)}+\frac{(\mathbf{k}_{12}\times\mathbf{k}_{31})^2}{\big(k_{12}^2+m_\pi^2\big)\big(k_{31}^2+m_\pi^2\big)}+\frac{(\mathbf{k}_{23}\times\mathbf{k}_{31})^2}{\big(k_{23}^2+m_\pi^2\big)\big(k_{31}^2+m_\pi^2\big)}\right]\Bigg).\end{aligned} \tag{B17}$$

2. V_D contribution

To calculate $\langle 123|\mathcal{A}_{123}V_D|123\rangle$, we first consider the isospin part, which is of the $G^{(1)}$ form. Using the results from Eq. (B12), we find for the matrix element, dropping terms that give nonvanishing contributions after summing over spins,

$$\begin{aligned}\langle nnp|\,\mathcal{A}_{123}V_D\,|nnp\rangle &= 2\big[-P_{12}^{\sigma k}d_{12} - 2P_{13}^{\sigma k}d_{13} - 2P_{23}^{\sigma k}d_{23}\\&+2P_{13}^{\sigma k}P_{23}^{\sigma k}d_{23} + 2P_{13}^{\sigma k}P_{23}^{\sigma k}d_{13}\big],\end{aligned} \tag{B18}$$

where

$$d_{ij} = -\frac{g_A}{8F_\pi^2}\frac{c_D}{F_\pi^2\Lambda_\chi}\frac{\boldsymbol{\sigma}_j\cdot\mathbf{q}_j}{q_j^2+m_\pi^2}(\boldsymbol{\sigma}_i\cdot\mathbf{q}_j). \tag{B19}$$

Summing over spins leaves terms like

$$\frac{1}{4}(1+\boldsymbol{\sigma}_1\cdot\boldsymbol{\sigma}_2)(1+\boldsymbol{\sigma}_2\cdot\boldsymbol{\sigma}_3)d_{23}\xrightarrow{\text{Tr}} 2\,\mathbf{q}_2^2. \tag{B20}$$

Finally, evaluating the momentum-exchange operators, we find for the V_D contribution to the Hartree-Fock energy density,

$$\begin{aligned}\left.\frac{E_{V_D}^{(1)}}{V}\right|_{nnp} &= \frac{g_A}{6F_\pi^2}\frac{c_D}{F_\pi^2\Lambda_\chi}\int\frac{d\mathbf{k}_1 d\mathbf{k}_2 d\mathbf{k}_3}{(2\pi)^9}\,n_{\mathbf{k}_1}^n n_{\mathbf{k}_2}^n n_{\mathbf{k}_3}^p\,f_{\mathrm{R}}^2\\&\times\left[\frac{k_{12}^2}{k_{12}^2+m_\pi^2}+\frac{k_{23}^2}{k_{23}^2+m_\pi^2}+\frac{k_{13}^2}{k_{13}^2+m_\pi^2}\right].\end{aligned} \tag{B21}$$

3. V_E contribution

The isopin part of the matrix element $\langle 123|\mathcal{A}_{123}V_E|123\rangle$ is also of the $G^{(1)}$ form. Using the results from Eq. (B12) with $f_{ij}=1$, we have

$$\begin{aligned}&\langle nnp|\mathcal{A}_{123}\sum_{j\neq k}\boldsymbol{\tau}_j\cdot\boldsymbol{\tau}_k|nnp\rangle\\&= 2\big[-1+P_{12}^{\sigma k}-2P_{13}^{\sigma k}-2P_{23}^{\sigma k}\\&+2P_{12}^{\sigma k}P_{23}^{\sigma k}+2P_{13}^{\sigma k}P_{23}^{\sigma k}\big].\end{aligned} \tag{B22}$$

Summing over spins, only the 1/2 part of the spin-exchange operator $P_{ij}^{\sigma} = (1 + \boldsymbol{\sigma}_i \cdot \boldsymbol{\sigma}_j)/2$ gives nonvanishing contributions, so that the matrix element yields -24 after the spin traces. As a result, the V_E contribution to the Hartree-Fock energy density is given by

$$\left.\frac{E^{(1)}_{V_E}}{V}\right|_{nnp} = -2\frac{c_E}{F_\pi^4 \Lambda_\chi} \int \frac{d\mathbf{k}_1 d\mathbf{k}_2 d\mathbf{k}_3}{(2\pi)^9} n^n_{\mathbf{k}_1} n^n_{\mathbf{k}_2} n^p_{\mathbf{k}_3} f_{\mathrm{R}}^2. \quad \text{(B23)}$$

[1] K. A. Brueckner, S. A. Coon, and J. Dabrowski, Phys. Rev. **168**, 1184 (1968).
[2] I. E. Lagaris and V. R. Pandharipande, Nucl. Phys. A **369**, 470 (1981).
[3] I. Bombaci and U. Lombardo, Phys. Rev. C **44**, 1892 (1991).
[4] W. Zuo, I. Bombaci, and U. Lombardo, Phys. Rev. C **60**, 024605 (1999).
[5] W. Zuo, A. Lejeune, U. Lombardo, and J. F. Mathiot, Eur. Phys. J. A **14**, 469 (2002).
[6] I. Vidaña, C. Providência, A. Polls, and A. Rios, Phys. Rev. C **80**, 045806 (2009).
[7] S. Fantoni, S. Gandolfi, A. Y. Illarionov, K. E. Schmidt, and F. Pederiva, AIP Conf. Proc. **1056**, 233 (2008).
[8] T. Frick, H. Müther, A. Rios, A. Polls, and A. Ramos, Phys. Rev. C **71**, 014313 (2005).
[9] E. Epelbaum, H.-W. Hammer, and U.-G. Meißner, Rev. Mod. Phys. **81**, 1773 (2009).
[10] S. K. Bogner, R. J. Furnstahl, and A. Schwenk, Prog. Part. Nucl. Phys. **65**, 94 (2010).
[11] H.-W. Hammer, A. Nogga, and A. Schwenk, Rev. Mod. Phys. **85**, 197 (2013).
[12] K. Hebeler and A. Schwenk, Phys. Rev. C **82**, 014314 (2010).
[13] S. K. Bogner, A. Schwenk, R. J. Furnstahl, and A. Nogga, Nucl. Phys. A **763**, 59 (2005).
[14] A. Gezerlis, I. Tews, E. Epelbaum, S. Gandolfi, K. Hebeler, A. Nogga, and A. Schwenk, Phys. Rev. Lett. **111**, 032501 (2013).
[15] K. Hebeler, S. K. Bogner, R. J. Furnstahl, A. Nogga, and A. Schwenk, Phys. Rev. C **83**, 031301 (2011).
[16] N. Kaiser, S. Fritsch, and W. Weise, Nucl. Phys. A **697**, 255 (2002).
[17] A. Lacour, J. A. Oller, and U.-G. Meißner, Ann. Phys. **326**, 241 (2011).
[18] S. Fiorilla, N. Kaiser, and W. Weise, Nucl. Phys. A **880**, 65 (2012).
[19] J. W. Holt, N. Kaiser, and W. Weise, arXiv:1304.6350.
[20] E. Epelbaum, H. Krebs, D. Lee, and U.-G. Meißner, Eur. Phys. J. A **40**, 199 (2009).
[21] A. Carbone, A. Polls, and A. Rios, Phys. Rev. C **88**, 044302 (2013).
[22] I. Tews, T. Krüger, K. Hebeler, and A. Schwenk, Phys. Rev. Lett. **110**, 032504 (2013).
[23] T. Krüger, I. Tews, K. Hebeler, and A. Schwenk, Phys. Rev. C **88**, 025802 (2013).
[24] K. Hebeler, J. M. Lattimer, C. J. Pethick, and A. Schwenk, Astrophys. J. **773**, 11 (2013).
[25] R. Machleidt and D. R. Entem, Phys. Rep. **503**, 1 (2011).
[26] D. R. Entem and R. Machleidt, Phys. Rev. C **68**, 041001 (2003).
[27] S. K. Bogner, R. J. Furnstahl, S. Ramanan, and A. Schwenk, Nucl. Phys. A **784**, 79 (2007).
[28] U. van Kolck, Phys. Rev. C **49**, 2932 (1994).
[29] E. Epelbaum, A. Nogga, W. Glöckle, H. Kamada, Ulf-G. Meißner, and H. Witała, Phys. Rev. C **66**, 064001 (2002).
[30] T. Otsuka, T. Suzuki, J. D. Holt, A. Schwenk, and Y. Akaishi, Phys. Rev. Lett. **105**, 032501 (2010).
[31] J. D. Holt, T. Otsuka, A. Schwenk, and T. Suzuki, J. Phys. G **39**, 085111 (2012).
[32] A. T. Gallant *et al.*, Phys. Rev. Lett. **109**, 032506 (2012).
[33] F. Wienholtz *et al.*, Nature **498**, 346 (2013).
[34] E. Epelbaum, W. Glöckle, and U.-G. Meißner, Nucl. Phys. A **747**, 362 (2005).
[35] M. C. M. Rentmeester, R. G. E. Timmermans, and J. J. de Swart, Phys. Rev. C **67**, 044001 (2003).
[36] K. Hebeler, Phys. Rev. C **85**, 021002 (2012).
[37] K. Hebeler and R. J. Furnstahl, Phys. Rev. C **87**, 031302 (2013).
[38] W. Zuo, J. Phys.: Conf. Ser. **420**, 012089 (2013).
[39] P. Grange, A. Lejeune, M. Martzolff, and J. F. Mathiot, Phys. Rev. C **40**, 1040 (1989).
[40] A. Akmal, V. R. Pandharipande, and D. G. Ravenhall, Phys. Rev. C **58**, 1804 (1998).
[41] G. Taranto, M. Baldo, and G. F. Burgio, Phys. Rev. C **87**, 045803 (2013).
[42] P. Danielewicz and J. Lee, Nucl. Phys. A **922**, 1 (2014).
[43] K. Hebeler, J. M. Lattimer, C. J. Pethick, and A. Schwenk, Phys. Rev. Lett. **105**, 161102 (2010).
[44] A. Schwenk, B. Friman, and G. E. Brown, Nucl. Phys. A **713**, 191 (2003).
[45] A. Bauswein, H.-T. Janka, K. Hebeler, and A. Schwenk, Phys. Rev. D **86**, 063001 (2012).